Topologically protected states and half-metal behaviors: Defect-strain synergy effects in two-dimensional antimonene

Ziyu Hu,[1] Junfeng Gao,[2,*] Shengli Zhang,[3,†] Jijun Zhao,[2] Wenhan Zhou,[3] and Haibo Zeng[3]

[1]*College of Mathematics and Physics, Beijing University of Chemical Technology, Beijing 100029, People's Republic of China*

[2]*Laboratory of Materials Modification by Laser, Ion and Electron Beams, Dalian University of Technology, Ministry of Education, Dalian 116024, China*

[3]*Key Laboratory of Advanced Display Materials and Devices, Ministry of Industry and Information Technology, College of Material Science and Engineering, Nanjing University of Science and Technology, Nanjing 210094, China*

(Received 12 March 2019; revised manuscript received 23 May 2019; published 22 July 2019)

Two-dimensional (2D) materials often feature defects and strain, due to their atomic layered character, which can cause problems for applications. Antimonene, a monolayer material derived from layered bulk Sb, undergoes a semiconductor-to-topological-insulator transition under large strain. However, it is unclear whether the structure and properties of antimonene are retained under strain once defects are generated. Here, we used *ab initio* calculations to explore a series of the most probable defects in these materials, including the Stone-Wales (SW) defects, single vacancies, double vacancies (DV), and adatoms. Interestingly, the influence of defects can be categorized into two types: for defects involving the loss/addition of an odd number of atoms, the material becomes ferromagnetic and exhibits half-metal properties under a certain strain; for defects involving an even number of missing atoms, the material remains a nonmagnetic semiconductor. Moreover, the topological phase transitions are robust for Sb monolayers with SW defects, but the critical transition strain decreases. Conversely, topological phase transitions might vanish for DV (555|777) and DV (5|8|5) defects. Our calculations suggest that different types of defects and strain might transform antimonene into a semiconductor, half-metal, or topological insulator. Therefore, defects and strain effects in antimonene should be carefully controlled for its applications.

DOI: 10.1103/PhysRevMaterials.3.074005

I. INTRODUCTION

Two-dimensional (2D) materials have thin atomic layers, which are associated with defects and strain that can cause problems for applications. However, defects and strain are also often useful for engineering the electronic/magnetic properties of 2D materials. Recently, a new family of 2D crystals, based on group-VA layered materials (phosphorene, arsenene, antimonene, and bismuth), has inspired considerable research interest because of their moderate band gaps [1–10], highly anisotropic transport [11–13], negative Poisson's ratio [1–3,14–18], excellent optical properties [11,19,20], and thermoelectric response [21–25]. Most importantly, 2D topological insulators (TIs) with large band gaps and small Poisson ratios have recently been predicted in layered materials of group VA (i.e., As, Sb, Bi, AsSb, AsBi, and SbBi) through strain engineering [26–31]. Such materials might be able to host quantum spin Hall (QSH) effects. Among these materials, antimonene, formed from monolayers of layered bulk Sb, has been theoretically predicted [8,12,32] and experimentally synthesized [33–37]. This material has remarkable electronic properties, such as high carrier mobilities [8] and large-band-gap 2D TI properties [34,38–40], and it supports high-temperature applications [41].

As strain increases, monolayer Sb and its compound AsSb can host metallic edge states protected by mirror symmetry and surpass an inverted gap, i.e., the semiconducting monolayer Sb transforms into a typical topological insulator at a critical strain [28]. These theoretically predicted monolayer materials are often represented without defects; however, it is difficult to eliminate the various defects during synthesis and device fabrication. Some typical point defects include adatoms (AD), Stone-Wales (SW) defects, single vacancies (SV), and double vacancies (DV), which are commonly observed in other 2D materials, such as graphene and silicene [42–49]. The defects may reduce the modulus of antimonene, resulting in it breaking up before the critical strain. Furthermore, defects might also considerably alter intrinsic electronic/magnetic properties of antimonene, a phenomenon that has also been found in graphene, silicene [50], and other 2D materials. Thus, we should consider the influence of defects in antimonene and whether the topolectal insulator transformation is robust in defective antimonene. It is also possible that new electronic/magnetic properties might be introduced by typical defects under variable strain. To answer these questions, we must systemically explore the structures, evolution behaviors, and the properties of typical defects in antimonene under a range of strain values.

In this paper, we systematically investigated typical point defects including AD, several SV, DV, and SW transformations. We found that these defective structures are more complex than those of graphene and silicene. We simulated their atomic structures with a simulated scanning tunneling

*Author to whom all correspondence should be addressed: gaojf@dlut.edu.cn

†zhangslvip@njust.edu.cn

microscope (STM), and our findings will be useful for experimental identification of this material in the future. Furthermore, we studied their formation energies, kinetic migration barriers, and transformation behaviors. We showed that DV(555|777) is more stable than SV defects without strain, whereas AD are the most energetically unfavorable in antimonene and very different from silicene with similar buckling structures. The stability of the defects can be altered by external strain, which suggests that defects might be controlled by annealing under a certain strain. The effects on electronic/magnetic properties are highly dependent on the number of atoms involved in the defects. Defects involving an odd number of atoms, such as an SV defect (one atom) and AD (one atom), transform semiconducting antimonene into a ferromagnetic metal, which can further transform into a half-metal under small strain. In contrast, defects with an even number of atoms maintain a similar character to that of pristine antimonene. Structures containing DV(555|777) and SW defects exhibit topological state transformations; however, their critical strain is lower than that of pristine antimonene. DV(5|8|5) has a higher formation energy than that of (555|777), and the topological state transformation disappears because it is broken up before the critical strain. Therefore, applications of antimonene should consider defect-strain control, which might be achieved by annealing under a selected strain.

II. COMPUTIONAL DETAILS

The calculations were performed in the Vienna *Ab initio* Simulation Package (VASP) [51]. The exchange-correlation term is described within the generalized gradient approximation (GGA) parametrized by the Perdew-Burke-Ernzerhof (PBE) functional [52]. A vacuum region greater than 20 Å perpendicular to the sheets (along the *c*-axis) was applied to avoid interaction between layers caused by the periodic boundary condition (PBC). For geometry optimization, the kinetic-energy cutoff for plane-wave expansion was set to be 400 eV. All the atoms in the unit cell were fully relaxed until the force on each atom was less than 0.01 eV/Å. Electronic minimization was performed with a tolerance of 10^{-5} eV. The Brillouin-zone sampling was performed with a $9 \times 9 \times 1$ Monkhorst-Pack [53] grid for all the 2D sheets with defects. The PBE calculations used scalar-relativistic PAW potentials, where both the core and the valence orbitals were treated using a scalar relativistic Hamiltonian. The climbing-image nudged elastic band method (*c*-NEB) was used to locate the transition states to study defect migration [54]. Spin-orbital coupling (SOC) effects were included self-consistently up to second order (LS coupling) [55]. Because the SOC term is large close to the core, the corresponding contributions to the Hamiltonian were only evaluated inside the PAW spheres by all-electron partial waves.

III. RESULTS AND DISCUSSION

A. Structures and simulated STM images of defects in *h*-Sb monolayers

To explicitly evaluate the structures and stabilities of defects in antimonene, we constructed a series of hexagonal and rectangle supercells for SW, SV, DV, and AD defects

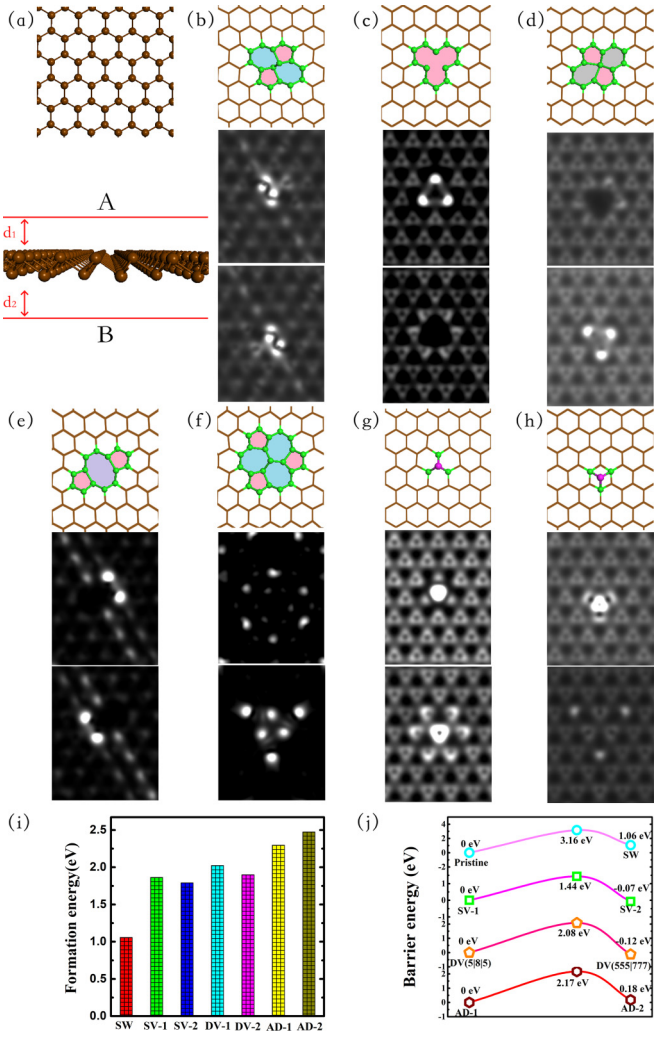

FIG. 1. Optimized structural configurations of monolayer for (a) perfect, (b) Stone-Wales defect (55|77, SW), (c) single vacancy with one missing Sb atom (5|7, SV-1), (d) single vacancy with one missing Sb atom (55|77, SV-2), (e) double vacancies (5|8|5, DV-1), (f) double vacancies (555|777, DV-2), (g) adatom (top site) in *h*-Sb (AD-1), and (h) adatom (hollow site) in *h*-Sb (AD-2). Atomic structures together with simulated STM images for (a)–(h) defects in *h*-Sb, which are displayed in both top-views and below-views from two horizontal directions. All the STM images were simulated at a voltage of 2.0 V between the tip and the sample. (i) Structural stability of the defects, and formation energies (E_f) of the $4\sqrt{3} \times 6$ defect containing cells are listed in the lower rows. (j) Energy barriers for the transformation pristine to SW defect, SV diffusion, DV(5|8|5) to DV(555|777), for AD-1 to AD-2 in *h*-Sb.

in antimonene, as shown in Figs. 1(a)–1(h) and Figs. S1(a)–S1(h) within the Supplemental Material [56]. Figure 1(a) shows that pristine antimonene has a buckling honeycombed structure, similar to that of silicene. After structure relaxation, we find that two SV, one SW, two DV, and two AD defects are stable in antimonene. SV-1 [Fig. 1(b)] is composed of 5|5|7|7-membered rings, whereas SV-2 retains all Sb atomic positions but is missing one Sb atom from its center. The 5|9 structure for SV in graphene is not stable in antimonene. Similar to graphene and silicene, DV can form 5|8|5 [DV-1,

see Fig. 1(e)] rings and reconstruct to a 5|5|5|7|7|7 [DV-2, see Fig. 1(f)] structure. AD-1 [Fig. 1(g)] is on the top site of the Sb atoms, which is a similar arrangement to that in silicene. AD-2 [Fig. 1(h)] is located on the hollow site. The bridge site, which is the most stable site for AD in graphene, is not stable for AD in antimonene.

To provide visible guidance for experimental observations, we simulated the scanning tunneling microscopy (STM) images of explored structures. As shown in Fig. 1, there are two sides for antimonene (labeled here as A for the top and B for the bottom sides). The STM images were simulated under a voltage of 2.0 V and the tip was approximately 2 Å away from each side, separately. Notably, the symmetry of the defects in antimonene was broken by buckling of the structure. Therefore, the distribution of the bright spots from the A and B sides was quite different except for the SW defects. As shown in Figs. 1(b)–1(h), the STM images were more complex than those of graphene. Thus, it is difficult to determine the atomic structures from the STM images. Our simulation results might assist in recognizing these defects in experiments.

To qualitatively assess the stabilities of defective *h*-Sb monolayers, their formation energies are calculated by

$$E_f{}^{\mathrm{Sb}} = E_t{}^{\mathrm{Sb}} - nE_{\mathrm{atom}}{}^{\mathrm{Sb}},$$

where $E_t{}^{\mathrm{Sb}}$ is the total energy of the defective *h*-Sb monolayer, $nE_{\mathrm{atom}}{}^{\mathrm{Sb}}$ is the energy of n Sb atoms in the defect structures, n is the number of Sb atoms in the defective supercells, and $E_{\mathrm{atom}}{}^{\mathrm{Sb}}$ is the energy per Sb atom in perfect antimonene. Furthermore, the formation energy might be influenced by the density and arrangement of defects in antimonene. Therefore, we calculated the formation of each defect with a series of rectangular and triangular supercells of different sizes. These results are shown in Figs. S1(a)–S1(h) within the Supplemental Material [56]. The formation energies almost converged for $4\sqrt{3} \times 6$ supercells. Therefore, we selected a $4\sqrt{3} \times 6$ supercell to further study the stability and properties of each defect.

B. Stabilities and mobilities of defects in *h*-Sb monolayers

The formation energies for each defect in the square $4\sqrt{3} \times 6$ supercell are shown in Fig. 1(i) and summarized in Table I. The calculated formation energies and band gaps for all types of point defects are compared with those of arsenene (*h*-As) and silicene (Si). The formation energies of each defect in the *h*-Sb monolayer (1.06–2.47 eV) were systemically lower than that in *h*-As (1.30–2.98 eV) and silicene (2.09–3.90 eV) [50,57]. Hence, defects are likely to form more easily in *h*-Sb than in *h*-As and silicene. Thereby, the defects in *h*-Sb should be considered.

The ground-state structure of SV is the SV-2(55-77) structure, which has a formation energy of 1.79 eV (i.e., 0.07 eV lower than that of SV-1). Similar to graphene and silicene, the initial DV-1 (5|8|5) defect is likely to transform into DV-2(555|777), lowering the formation energy by 0.12 eV. The formation energy of DV-2 is 1.90 eV, which is approximately 1.68 eV lower than that of the two isolated SV-2s, implying that DV-2 is more thermodynamically stable than the two isolated SVs. For AD defects, we carefully check all the configurations: top, bridge, or hollow positions shown in Fig. S2 within the Supplemental Material [56]. The most stable configuration is on the top position, which is the same as the result of buckled silicene [50]. But it is different from graphene, in which the most stable position is the bridge one [42]. The formation energy of the AD defect at the hollow site was only 0.18 eV higher than that at the top site. We note that the formation energy per atom for AD was highest among all the explored defects. This result is similar to that of graphene, but very different from that of silicene, for which AD defects are energetically favored. Therefore, we infer that the atomic monolayer of *h*-Sb is more stable than that of silicene.

To understand the kinetics of defects in antimonene, we systematically investigated their migration/transformation barriers and paths by first-principles calculations; detailed results are shown in Fig. 1(j) and Fig. S3 within the supplemental material [56]. To generate the SW defects from pristine antimonene, the 3.16 eV barrier for bond rotation must be overcome. This value is approximately 1/3 that of graphene (∼10 eV). Because SW defects are indeed observed in graphene, it might also exist in *h*-Sb.

The diffusion of SV was accompanied by a transformation between SV-1(55|77) and SV-2. The transformation barrier was 1.44 eV. The diffusion barrier of SV was slightly higher than that in graphene but only half as high as that in MoS_2. DV-585 is the initial DV with two missing Sb atoms. By overcoming the 2.08 eV barrier, the defect can reconstruct into DV-555|777 (see Fig. S3 within the Supplemental Material [56]). For a surface AD, diffusion from AD-1 to AD-2 must overcome a 2.17 eV barrier. The energy barrier of these defects is in the range of 1.44–2.17 eV, except for the SW defect. We can evaluate the mobility of a defect in *h*-Sb with

TABLE I. Calculated formation energies for various point defects in buckled antimonide. For comparison, the corresponding values of arsenene and silicene are also listed. g is the band gap value of Sb polymorphs calculated by PBE, PBE+SOC, HSE, and HSE+SOC. μ_B is the total magnetic moment.

Defects	$E_f{}^{\mathrm{Sb}}$(eV)	$E_f{}^{\mathrm{As}}$(eV)	$E_f{}^{\mathrm{Si}}$(eV)	g^{PBE}	$g^{\mathrm{SOC+PBE}}$	g^{HSE}	$g^{\mathrm{HSE+SOC}}$	μ_B
SW	1.06	1.30	2.09[50]	1.04	0.88	1.42	1.16	0
DV(5|8|5)	2.02	2.39	3.70[50]	0.84	0.61	1.23	0.98	0
DV(555|777)	1.90	1.97	2.84[50]	1.23	1.05	1.63	1.34	0
SV-1	1.86	2.13	3.77[50]	0	0	0	0	0.87
SV-2	1.79	2.14		0	0	0	0	0.23
AD-1	2.29	2.91	3.90[50]	0	0	0	0	3.19
AD-2	2.47	2.98		0	0	0	0	3.17

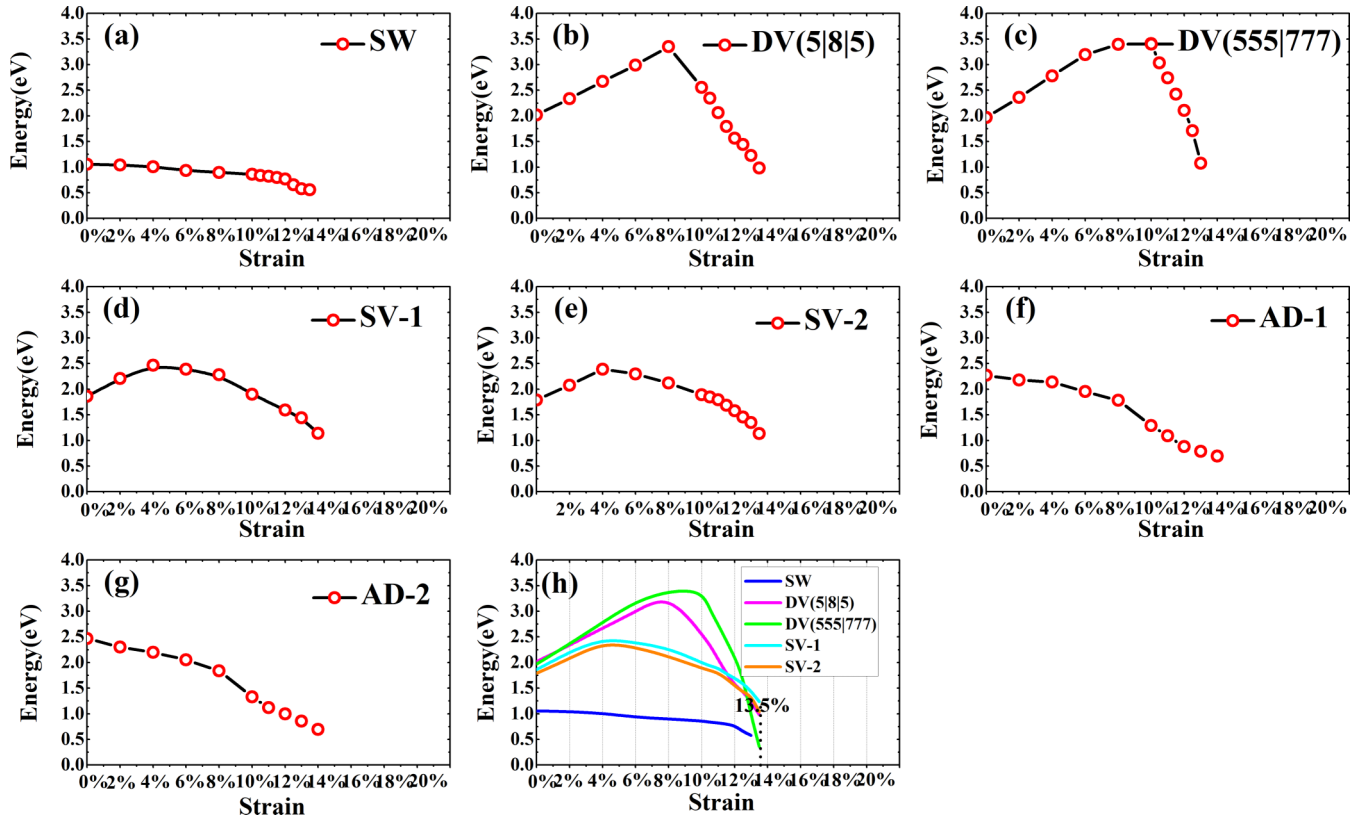

FIG. 2. Formation energy of (a) SW (55|77, SW), (b) DV-1 (5-8-5), (c) DV-2 (555|777) SV-1 (d), SV-2 (e), AD-1 (f), and AD-2 (g) under variable strain, respectively. (h) Comparison of formation energies of SW, SV-1/SV-2, and DV-1/DV-2.

the formula

$$R = \nu \exp\left(-E^*/kT\right),$$

where R is the transformation rate, ν is the bond vibration frequency in h-Sb, which is approximately 10^{13} for a solid, E^* is the energy barrier, k is the Boltzmann constant, and T is the temperature. Thus, the transformation rate for SV-1 is approximately 10^{-11} times per second at room temperature, which indicates that these defects show almost no movement at room temperature. This feature can ensure that devices based on these defects are stable. However, we can accurately control the transition by lifting the temperature. For example, the transition of SV is 10/s at 600 K and the transition rate of DV is approximately 6/s at 850 K.

C. Strain effects on the stabilities of defects in *h*-Sb monolayers

In real 2D devices, the 2D monolayer is strongly affected by tension. In particular, 2D h-Sb has a topological transition, which can be realized under approximately 14% tensile strain. To clarify the strain effects on defects in Sb structures, we plot the variation of the formation energies as a functional of biaxial strain before their fracturing in Fig. 2. As shown in Figs. 2(a), 2(f), and 2(g), the formation energies of SW, AD-1, and AD-2 defects gradually decreased before fracturing. However, for SV and DV defects, the formation energies first increased as strain increased. After reaching a critical strain (approximately 4% tension for SV and 8% tension for DV defects), further increases of strain reduced the formation energy.

As shown in Fig. 2(h), the stability of SV and DV defects can be tuned by strain. The formation energy of SV-2 is always the same as that for SV-1; however, the formation energy of the DV was altered. Without any strain, DV-2 (555|777) was more stable than DV-1 (5|8|5). However, DV-1 (5|8|5) was preferred at strain in the range from 2% to 8%. At strain greater than 8%, DV(555|777) became more stable than DV-1 (5|8|5). After 4% strain, the formation energies of the SVs began to decrease whereas the energies of DV defects continued to increase as strain increased. Below 8% strain, the formation energy of SV-2 was 2.11 eV, whereas the formation energies of DV-1 and DV-2 were 3.34 and 3.38 eV, respectively. By annealing the h-Sb under different strain, we might be able to tune the structure of the DV and the ratio between the DV and SV defects.

D. Fracture behaviors of defective *h*-Sb monolayers

Perfect antimonene is mechanically stable and can withstand a large strain up to 20% without fracturing. Strain is a powerful tool for tuning the electronic properties of antimonene. However, these defects can greatly affect the fracture behaviors of antimonene. To address this issue, we systemically investigated the fracture behaviors of defects in h-Sb.

As shown in Fig. 3, fracturing occurred at almost all defects, and the defects reduced the mechanical properties

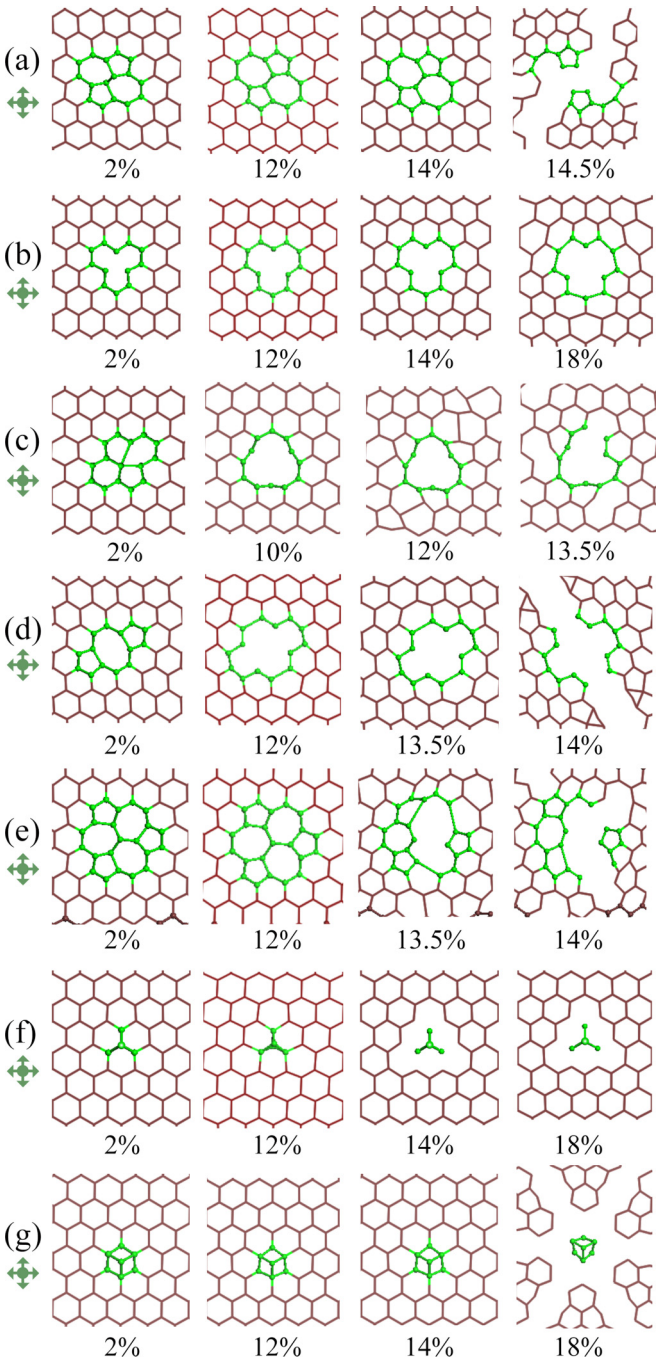

FIG. 3. Relaxed structures of SW (a), SV-1 (b), SV (55|77) (c), DV (5|8|5) (d), DV (555|777) (e), AD-1 (f), and AD-2 (g) defect Sb monolayers under biaxial strain in the range of 2%–20%. The left/right and up/down arrow icons under the captions of (a)–(g) indicate the directions of biaxial strain on the defect Sb monolayers.

of *h*-Sb. Most fracturing of defects occurred at close to 14% strain, except for the SV-1. Up to 12% strain, all the defect structures remained stable. After 13.5% strain, the structure of DV-2 became distorted whereas other defects remained stable. When the strain was 14%, the two DVs broke up. Furthermore, some local bonds at SV-2 and AD-1 were broken at 14% tension. Total rupture of SW and SV-2 defects occurred at 14.5% strain. Notably, AD-2 defects broke at 18% tension and SV-1 remained stable even at 18% strain.

E. Strain-induced band behaviors and quantum spin Hall insulators: SW and DV in *h*-Sb monolayers

One important feature of antimonene is a topological state transition in its band structure under approximately 14% strain. However, fracturing of defects mostly occurred at 14% in tension. Thus, we consider the effects of defects on the electronic properties of antimonene and whether the topological state transition can survive in defective antimonene. Furthermore, we consider if any new properties and applications might be introduced by defects.

We further explored the electronic/magnetic properties of all defects. The band gaps for the SW, DV-5|8|5, and DV-555|777 in *h*-Sb calculated at the PBE level with/without spin-orbital coupling (SOC) are listed in Table I, and detailed band structures are shown in Fig. S4 within the Supplemental Material [56]. The electronic states were divided into two types: (i) among SW defect materials, DV-5|8|5 and DV-555|777 defects, having an even number of missing atoms, are nonmagnetic semiconducting; (ii) materials with SV-5|7, SV-55|77, AD-1, and AD-2 defects, having an odd number of missing/additional atoms, show remarkable spin-polarized properties. The defects remained semiconducting but reduced the band gap. For perfect *h*-Sb, the band gap was 1.26 eV. For even defects, the band gap was in the range of 0.84–1.23 eV according to PBE calculations. These band gaps depend on the size of the supercell (density of defects) and we used a large enough supercell to nearly exclude interactions between neighboring defects, as shown in Fig. S1 within the Supplemental Material [56]. Taking the SOC effect into account, the band gaps changed to be 0.61–1.05 eV for even defects. Furthermore, we also used HSE to check the band structures. The band gaps of even defect structures were between 1.23 and 1.63 eV without SOC by HSE methods, and 0.98 and 1.34 eV with SOC. Although the band gaps calculated by HSE were systemically larger than those calculated by PBE, the overall trend was unchanged. This result implies that standard PBE is able to resolve the semiconducting and metallic band structures and their band trends. In the following, we will study the electronic properties under different strain. Because of the difficulty of calculating at the HSE level and the large number of structures, we used standard PBE with/without SOC to study the change of the band structures under different strain.

The band gaps and partial charge density of the valence-band maximum (VBM) and conduction-band minimum (CBM) for even defects [SW, DV-1(5|8|5), and DV-2(555|777)] in *h*-Sb monolayers are listed in Fig. S4 within the Supplemental Material [56]. Among these, the DV-2(555|777) defects possessed a direct band gap, whereas others had indirect band gaps. The shrinkage of the band gap originates from the defects. Unlike *h*-As and Si monolayers [50,57], the CBM values of even defects were localized at inner defective sites, whereas the charge of the VBM was localized around defects.

Strain-induced band inversion in perfect antimonene led to a nontrivial topological phase at ∼14% tension, and also

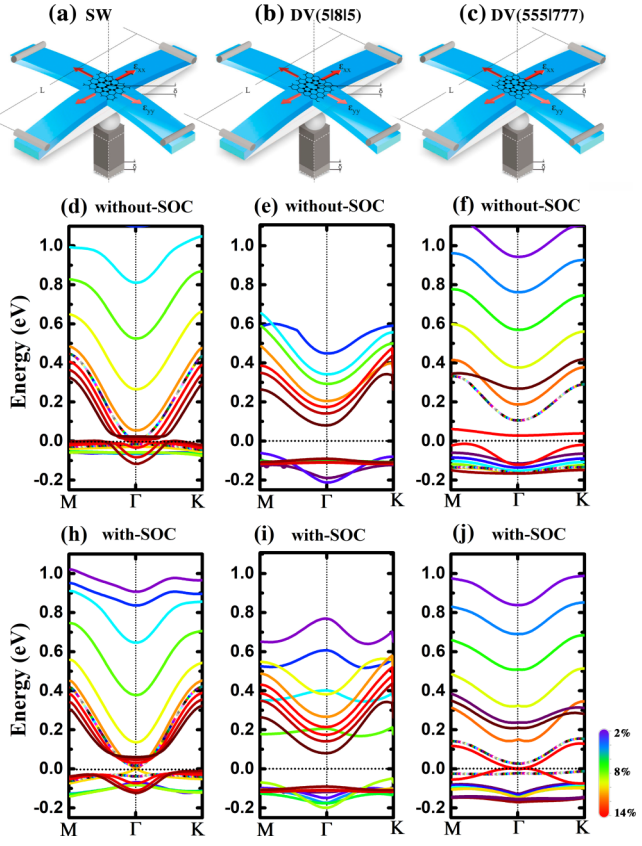

FIG. 4. Schematic illustration of biaxial strain apparatus (a) for SW, (b) for DV(5|8|5), and (c) for DV(555|777). Electronic band structures of (d),(h) Stone-Wales defects (55|77, SW); (e),(i) double vacancies (5|85, DV-1); and (f),(j) double vacancies (555|777, DV-2) in *h*-Sb monolayer under biaxial tensile strain at PBE level of theory without and with SOC. Horizontal dashed lines indicate the Fermi level. For PBE without SOC, the band gaps of SW defects closed at $\varepsilon = 12.5\%$ and reopened with an associated change of the band shape, which is reminiscent of band inversion and characteristic of many known TIs. The band gap of DV(555|777) and DV(5|8|5) did not close until $\varepsilon = 14\%$, before its structure was corrupted. For PBE with SOC the band gaps of SW defects and DV(555|777) closed at $\varepsilon = 12\%$ and reopened with an associated change of the band shape. The band gap of DV(5|8|5) did not close until $\varepsilon = 14\%$, before its structure was corrupted.

the topological state transition can survive in defective antimonene with the increase of tensile strain. In this regard, considering SOC effect which has been successfully achieved in silicene [58] and stanene [59], we use the same methods investigated the effects of defects on the electronic and topological properties of antimonene. As shown in Figs. 4(a)–4(c), pressing the plastic substrate with a cruciform shape caused symmetrical deformation around its center, thus inducing a biaxial strain at the purposed position. Uniaxial and biaxial tensile testing is easily applied to 2D materials. Furthermore, it can be applied in a stepwise and controllable manner, with direct measurements by strain gauges. With consideration of this method, we systemically investigated the electronic properties of SW [Fig. 4(a)], DV-585 [Fig. 4(b)], and DV-555|777 [Fig. 4(c)] defects in *h*-Sb monolayers under different strain. Their first conductive band-1 (CB-1, the lowest-energy conductive band) and valence band-1 (VB-1, the highest-energy valence band) of SW, DV-1(5|8|5), and DV-2(555|777) defect structures under different strain ranging from 2% to 14% calculated at the PBE level with (without) spin-orbital coupling (SOC) are shown in Figs. 4(d)–4(f) [Figs. 4(h)–4(j)]. The exact band-gap values and their changes are shown in Figs. S5(a)–S5(c) (with SOC) within the Supplemental Material [56], and the band-gap structures under some typical strain values are shown in Figs. S6–S8 (with SOC) within the Supplemental Material [56].

Comparing the indirect band gap of SW without tension calculated at the PBE level without SOC, a strain of only 2% transformed it into a direct band gap at the Γ point. This indirect-to-direct band-gap transition suggests that strain can alter optical and photoelectric properties. As the biaxial stress stain increased, the CB moved toward the Fermi level [as shown in Fig. 4(d)]. For clear demonstrations, we only plotted the shift of the CB-1 and VB-1 bands from 2% to 14%, as shown in Fig. 4(d). Under a strain of 12.5%, the CBM and VBM contracted at the Γ point. Further increases of the strain reversed the band polarity before the structure fractured. This behavior is similar to that of perfect *h*-Sb; however, the SW promoted this topological transition ahead of strain.

As the stain increased to 12%, the band gap for the DV-1(5|8|5) calculated at the PBE level without SOC transformed to a direct band gap, and increasing strain reduced the band gap. The CB-1s and VB-1s energy levels of DV-1(5|8|5) under biaxial stress strain from 2% to 14% are shown in Fig. 4(e). Unlike the SW defects, the CBM and VBM did not contract for DV-1(5|8|5), and the unique band gap remained around its fracture point.

The changes of CB-1 and VB-1 to DV-2 (555|777) calculated at the PBE level without SOC are similar to those for the DV-1(5|8|5) defects. Although the contraction between the CBM and VBM failed for DV-1(5|8|5) and DV-2 (555|777) under 12% strain [as shown in Fig. 4(f)], contraction was maintained for SW under 12.5% strain. Thus, to maintain the topological state transition in the band structures, careful structural control and annealing is required for *h*-Sb.

Comparing the band gaps calculated at the PBE level without SOC, and the indirect band gap calculated at the PBE level with SOC of SW without tension, a strain of 2% also transformed it into a direct band gap at the Γ point. As the biaxial stress stain increased, the CB moved toward the Fermi level [as shown in Fig. 4(h) and Fig. S6 within the Supplemental Material [56]]. For clear demonstrations, we also plotted the shift of the CB-1 and VB-1 bands from 2% to 14%, as shown in Fig. 4(h). Under a strain of 12%, the CBM and VBM contracted at the Γ point. Further increases of the strain reversed the band polarity before the structure fractured. This behavior is similar to that of perfect *h*-Sb; however, the SW promoted this topological transition to 12% strain.

Similar to the case without SOC, the DV-1(5|8|5) calculated at the PBE level with SOC also had an indirect band gap with a CBM in between the Γ-*K* direction and the VBM was at the *M* or *K* point before a strain of 12% (as shown in Fig. S7 within the Supplemental Material [56]). As the stain increased to 12%, the band gap transformed to a direct band gap, and increasing strain reduced the band gap. The CB-1

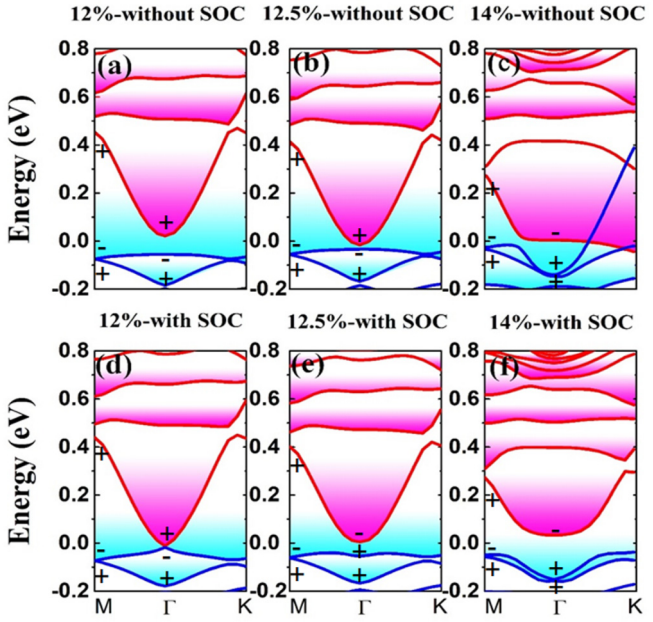

FIG. 5. Electronic band structures of Stone-Wales (55|77, SW) defect of antimonene under different tensile strain (12%, 12.5%, and 14%) obtained from DFT calculations at PBE level of theory (a)–(c) without SOC and (d),(e) with SOC effect. The energy at the Fermi level was set to be zero. The signs (+/−) in (a)–(f) indicate the parities of the wave functions at the Γ and *M* points.

and VB-1 energy levels of DV-1(5|8|5) under biaxial stress strain from 2% to 14% are shown in Fig. 4(i). Unlike the perfect *h*-Sb and SW defects, the CBM and VBM did not contract for DV-1(5|8|5) and the unique band gap remained around its fracture point. Although the contraction between the CBM and VBM failed for DV-1(5|8|5) and DV-2 (555|777) in the case without SOC, contraction for DV-2 (555|777) was maintained for under 12% strain [as shown in Fig. S8 within the Supplemental Material [56] and Fig. 4(j)].

To further confirm the topological nontriviality of stretched antimonene, we checked the topological invariant Z_2 for SW [28,60]. To gain physical insights into the band inversion that reflect the topological properties, we explicitly evaluated the band-structure evolution at the Γ and *M* points based on the methods proposed by Fu and Kane [61,62] [as shown in Figs. 5(a)–5(f)]. The honeycomb lattices of SW (55|77) defect antimonene had four time-reversal-invariant momenta at the points of $\Gamma_i = n_1\vec{b_1} + n_2\vec{b_2}$, with $\vec{b_1}$ and $\vec{b_2}$ being the basis vectors of the reciprocal lattice and n_1, $n_2 \epsilon \{0, 1/2\}$. The Z_2 invariant ν is defined by

$$(-1)^{\nu} = \prod_{\mathrm{i}} \delta_{\mathrm{i}} \text{ with } \delta_{\mathrm{i}} = \prod_{m=1}^{N} \xi_{2m}(\Gamma_i)$$

for $2N$ occupied bands. $\xi(\Gamma) = \pm 1$ is the parity eigenvalue of the $2m$th occupied energy band at the time-reversal invariant momentum Γ_i. Our first-principles calculations showed that as the tensile strain decreased below the critical value of 12.5%, δ_i had values of (-), (-), (-), and (-) at (0, 0), (1/2, 0), (0, 1/2), and (1/2, 1/2) time-reversal momenta, respectively, leading to zero Z_2 invariant.

To clearly see the topological evolution of SW structure under strain, we added the comparison between the band structures without and with the SOC effect shown in Fig. 5. Under 12% tensile strain, the SW defect structure has normal band orders if the SOC effect is ignored, i.e., there is no band inversion [Fig. 5(a)] and the calculated $Z_2 = 0$. When the SOC effect is included, the conduction-band minimum (CBM) and valence-band maximum (VBM) touch each other, and the band gap is closed, as shown in Fig. 5(d). When increasing the tensile strain to 12.5%, the bands [Fig. 5(b)] without SOC still have trivial topology but a reduced band gap. However, under the SOC effect, the CBM and VBM exchange their band orders [Fig. 5(e)], and a nontrivial band gap is opened. The calculated $Z_2 = 1$. When increasing the tensile strain to 14%, there is a band inversion between CBM and VBM even though the SOC effect is not considered. But there is no gap because of the band crossing. If we consider the SOC effect, a large nontrivial gap is achieved. The signs (+ /−) in Figs. 5(a)–5(f) indicate the parities of the wave functions at the Γ and *M* points for SW defects at the time-reversal-invariant momenta, and their product for the two occupied bands under tensile strain of 10%, 12%, 12.5%, 13%, 13.5%, and 14% are listed in Table S1 within the Supplemental Material [56]. The (+) time-reversal momenta led to a topological invariant $Z_2 = 1$ beyond a strain of 12.5%, indicating that the strained SW [excepting DV(555|777) and DV(5|8|5)] defect containing antimonene remained topological insulators.

F. Half-metal SVs and DVs for spin electronics

The odd atomic defective *h*-Sb monolayers exhibited considerable magnetic properties. The magnetic moments were $0.87\mu_B$, $0.23\,\mu_B$, $3.19\,\mu_B$, and $3.23\,\mu_B$ for SV-1, SV-2, AD-1, and AD-2 per $4\sqrt{3} \times 6$ supercells, respectively. The moments for two ADs converged rapidly as the supercell size was increased. However, the magnetic moment is a very long-range interaction for two SVs. Although we used a very large supercell, the magnetic moment oscillated as the density of the SVs changed (see Fig. S1 within the Supplemental Material [56]).

The electronic/magnetic properties of odd defects were also very sensitive to strain. The formation energies under the stress of odd defects are presented in Fig. 2(h), and the corresponding band gap and magnetic moments are listed in Figs. S5(d)–S5(i) within the Supplemental Material [56]. The SV-1 defect structure remained until the strain increased to 20% and the formation energies continued to increase with further stress. Notably, the magnetic moment changed from $1\,\mu_B$ to $3\,\mu_B$, and the corresponding gap closed at strain in the ranges of 2%–4% and 12%–20%, and a 0.3 eV gap opened under stress in the range from 5% to 11%. Due to the SV-1 defect structure, SV-2 cracked at a stress of 15%. The formation energies and magnetic moments shared the same trend as that of SV-1 before the structure cracked. However, as stress was increased, the bandwidth of SV-2 from 0.3 eV gradually became 0 eV. For adatom defects, the AD-1 and AD-2 defect structures were all considered. The formation energies revealed an increase as the strain increased, and the magnetic moments showed a decreasing trend from $3\,\mu_B$ to $1\,\mu_B$. The corresponding bandwidth gradually decreased from

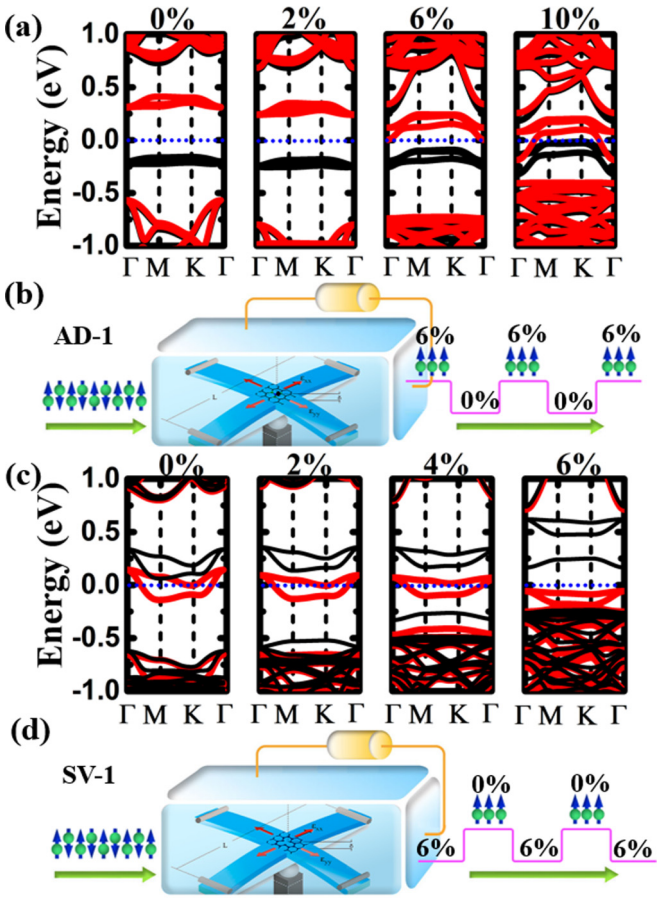

FIG. 6. Band gaps of AD-1 (a) and SV-1 (c) defects in *h*-Sb with the external biaxial strain ranging from 0% to 10%. Red and black lines indicate the spin-up and -down bands. Fermi levels are set at zero with light blue dots. Schematic diagrams of magnetic semiconductor manipulated spin corresponding to AD-1 (b) and SV-1 (d) defective *h*-Sb.

0.47 to 0 eV for AD-1 and from 0.49 to 0 eV for AD-2. The exact relaxed structures of even defects (SW, DV-5-8-5, and DV-555|777) and odd defects (SV-1, SV-2, AD-1, and AD-2) in *h*-Sb monolayers under biaxial strain from 2% to 20% are listed in Figs. S5(d)–S5(g) within the Supplemental Material [56]. The strained and collapsed structures indicate that external strain can efficiently modulate bond properties and electronic properties of *h*-Sb with even and odd defects.

When the magnetism and spin of a semiconductor can be controlled, it is possible to process, store, and transport information, thus providing a new conductive mode and device concept [63]. For example, in Fig. 6(a), pristine AD-1 is a semiconductor without any strain. External strain can shift its spin-up and spin-down band positions. Applying 2% strain clearly moves the CBM of the spin-up branch downward. Notably, the CBM of the spin-up band crosses the Fermi level at 6% strain, which makes thespin-up branch metallic, whereas the spin-down branch remains semiconducting. This half-metal phenomenon is rather robust over a wide tension range from approximately 6% to 10%. Strain greater than 10% makes the spin-up and spin-down bands metallic. Therefore, AD-1 defects in monolayer *h*-Sb generate a spin-electronic material. As shown in Fig. 6(b), AD-1 can filter the spin-polarized current by simply loading/reducing surface strain. At a strain of less than 6%, the AD-1 is a normally closed module. Under 6%–10% strain, AD-1 is open to a spin-up current but off for spin-down current. Hence, the spin-up current is injected by AD-1 filtering the nonpolar current. The AD-2 defect had similar behavior to AD-1, and details can be found in Fig. S9 within the Supplemental Material [56].

Similarly, SV defects can also exhibit half-metallic properties under certain strain. Here, we consider SV-1 in detail (a discussion of other defects can be found in Fig. S9 within the Supplemental Material [56]). As shown in Fig. 6(c), SV-1 is a normally open spin filter, which is only open to spin-up current but closed for spin-down current without tension. It is quite stable over a certain strain range from 0% to 6%. Strain greater than 6% will shut off all current because external strain induces an insulator transition by opening the band gaps for both the spin-up and -down bands. Therefore, SV-1 defects in the monolayer *h*-Sb can also be used to create a spin-electronic material. As shown in Fig. 6(d), SV-1 can also filter spin-polarized current by simply loading/removing surface strain; however, these defects show the opposite trend to that of AD-1. In the range of 0%–6% strain, SV-1 is open for the spin-up current but off for the spin-down current. At greater than 6% strain, the SV-1 is a normally closed module. The spin-up current is opened by the SV-1 filtering the nonpolar current.

IV. CONCLUSION

Pristine antimonene (*h*-Sb) has strong SOC effects and can be used as a topological insulator when highly strained. However, the stability of antimonene is changed by the presence of defects. Here we provide a comprehensive physical picture of the influence of point defects, their stabilities, and their properties under various strain. Typical point defects, such as the SW, SV, DV, and AD defects in *h*-Sb monolayer (antimonene), are all included. Their structures, stabilities, mobilities, and influences on electronic/magnetic properties were systemically evaluated by *ab initio* calculations. All these defects reduced the mechanical properties of *h*-Sb, and caused earlier fracturing. However, the critical strain of the topological phase transition was also reduced. For SW and DV (555|777), the topological phase transitions were retained and robust. The reduction of the critical transition stain promoted this stability. However, for DV (5|8|5) defects, fracturing occurred before the critical transition stain. We show that the AD and SV defects were spin-polarized and might act as good filters for spin-current injection, which can be easily controlled by loading/off the surface strain. Our theoretical results pave the way to understanding the formation, stability, and mechanical behaviors of defects in *h*-Sb and provide clear information for intentionally selecting defects for topological insulators and spin electronics. These findings will aid progress in device fabrication and applications of these materials.

ACKNOWLEDGMENTS

This work was financially supported by the National Natural Science Foundation of China (Grant No. 11604008)

and by BUCT Fund for Disciplines Construction (Project No. XK1702). J.G. gratefully acknowledges the Start-Up grant of DUT(3005-852069), and Natural Science Foundation of Jiangsu Province (BK20180071). We also acknowledge Computers at Tianhe2-JK in the Beijing Computational Science Research Center, and the computational support from the Supercomputing Center of Dalian University of Technology.

[1] L. Li, Y. Yu, G. J. Ye, Q. Ge, X. Ou, H. Wu, D. L. Feng, X. H. Chen, and Y. B. Zhang, Nat. Nanotechnol. **9**, 372 (2014).
[2] B. Anasori, M. R. Lukatskaya, and Y. Gogotsi, Nat. Rev. Mater. **2**, 16098 (2017).
[3] W. Y. Lei, G. Liu, J. Zhang, and M. H. Liu, Chem. Soc. Rev. **46**, 3492 (2017).
[4] J. W. Jiang and H. S. Park, Nat. Commun. **5**, 4727 (2017).
[5] D. Akinwande, N. Petrone, and J. Hone, Nat. Commun. **5**, 5678 (2014).
[6] F. Xia, H. Wang, and Y. Jia, Nat. Commun. **5**, 4458 (2014).
[7] R. Fei and L. Yang, Nano Lett. **14**, 2884 (2014).
[8] S. L. Zhang, Z. Yan, Y. F. Li, Z. F. Chen, and H. B. Zeng, Angew. Chem., Int. Ed. **127**, 3155 (2015).
[9] L. Kou, T. Frauenheim, and C. Chen, J. Phys. Chem. Lett. **5**, 2675 (2014).
[10] Q. Liu, X. Zhang, L. B. Abdalla, A. Fazzio, and A. Zunger, Nano Lett. **15**, 1222 (2015).
[11] J. Qiao, X. Kong, Z. X. Hu, F. Yang, and W. Ji, Nat. Commun. **5**, 4475 (2014).
[12] S. L. Zhang, M. Q. Xie, F. Y. Li, Z. Yan, Y. F. Li, E. J. Kan, W. Liu, Z. F. Chen, and H. B. Zeng, Angew. Chem., Int. Ed. **55**, 1666 (2016).
[13] G. Pizzi, M. Gibertini, E. Dib, N. Marzari, G. Iannaccone, and G. Fiori, Nat. Commun. **7**, 12585 (2016).
[14] M. Pumera and Z. Sofer, Adv. Mater. **29**, 1605299 (2017).
[15] T. Low, A. S. Rodin, A. Carvalho, Y. Jiang, H. Wang, F. Xia, and A. H. Castro Neto, Phys. Rev. B **90**, 075434 (2014).
[16] G. Qin, Q. B. Yan, Z. Qin, S. Y. Yue, and G. Su, Sci. Rep. **4**, 6946 (2014).
[17] S. L. Zhang, S. Y. Guo, Z. F. Chen, Y. L. Wang, H. J. Gao, J. Gómez-Herrero, P. Ares, F. Zamora, Z. Zhu, and H. B. Zeng, Chem. Soc. Rev. **47**, 982 (2018).
[18] H. Y. Zhang and J. W. Jiang, J. Phys. D **48**, 455305 (2015).
[19] V. Tran, R. Soklaski, Y. Liang, and L. Yang, Phys. Rev. B **89**, 235319 (2014).
[20] D. Singh, S. K. Gupta, Y. Sonvane, and Igor Lukačević, J. Mater. Chem. C **4**, 6386 (2016).
[21] M. Zeraati, S. Allaei, I. A. Sarsari, M. Pourfath, and D. Donadio, Phys. Rev. B **93**, 085424 (2016).
[22] Y. Aierken, D. Ćakır, C. Sevik, and F. M. Peeters, Phys. Rev. B **92**, 081408(R) (2015).
[23] Y. Cai, Q. Ke, G. Zhang, Y. P. Feng, V. B. Shenoy, and Y. W. Zhang, Adv. Funct. Mater. **25**, 2230 (2015).
[24] Z. Y. Ong, Y. Cai, G. Zhang, and Y. W. Zhang, J. Phys. Chem. C **118**, 25272 (2014).
[25] L. Zhu, G. Zhang, and B. Li, Phys. Rev. B **90**, 214302 (2014).
[26] S. L. Zhang, Y. H. Hu, Z. Y. Hu, B. Cai, and H. B. Zeng, Appl. Phys. Lett. **107**, 022102 (2015).
[27] H. J. Zhang, Y. D. Ma, and Z. F. Chen, Nanoscale **7**, 19152 (2015).
[28] M. Zhao, X. Zhang, and L. Li, Sci. Rep. **5**, 16108 (2015).
[29] S. L. Zhang, M. Q. Xie, B. Cai, H. J. Zhang, Y. D. Ma, Z. F. Chen, Z. Zhu, Z. Y. Hu, and H. B. Zeng, Phys. Rev. B **93**, 245303 (2016).
[30] S. L. Zhang, W. H. Zhou, Y. D. Ma, J. P. Ji, B. Cai, S. Y. A. Yang, Z. Zhu, Z. F. Chen, and H. B. Zeng, Nano Lett. **17**, 3434 (2017).
[31] S. S. Li, W. X. Ji, P. Li, S. J. Hu, L. Cai, C. W. Zhang, and S. S. Yan, ACS Appl. Mater. Interf. **9**, 21515 (2017).
[32] G. Wang, R. Pandey, and S. P. Karna, ACS Appl. Mater. Interf. **7**, 11490 (2015).
[33] M. Q. Xie, S. L. Zhang, B. Cai, Y. Gu, X. H. Liu, E. J. Kan, and H. B. Zeng, Nano Energy **38**, 561 (2017).
[34] J. P. Ji, X. F. Song, J. Z. Liu, Z. Yan, C. X. Huo, S. L. Zhang, M. Su, L. Liao, W. H. Wang, Z. H. Ni, Y. F. Hao, and H. B. Zeng, Nat. Commun. **7**, 13352 (2016).
[35] Y. Shao, Z. L. Liu, C. Cheng, X. Wu, H. Liu, C. Liu, J. Wang, S. Y. Zhu, Y. Q. Wang, D. X. Shi, K. Ibrahim, J. T. Sun, Y. Wang, and H. J. Gao, Nano Lett. **18**, 2133 (2018).
[36] C. Gibaja, D. Rodriguez San Miguel, P. Ares, J. Gomez Herrero, M. Varela, R. Gillen, J. Maultzsch, F. Hauke, A. Hirsch, G. Abellan, and F. Zamora, Angew. Chem., Int. Ed. **55**, 14345 (2016).
[37] M. Fortin Deschenes, O. Waller, T. O. Mentes, A. Locatelli, S. Mukherjee, F. Genuzio, P. L. Levesque, A. Hebert, R. Martel, and O. Moutanabbir, Nano Lett. **17**, 4970 (2017).
[38] P. Zhang, Z. Liu, W. Duan, F. Liu, and J. Wu, Phys. Rev. B **85**, 201410 (2012).
[39] G. Bian, T. Miller, and T. C. Chiang, Phys. Rev. Lett. **107**, 036802 (2011).
[40] G. Bian, X. Wang, Y. Liu, T. Miller, and T. C. Chiang, Phys. Rev. Lett. **108**, 176401 (2012).
[41] P. Ares, F. Aguilar Galindo, D. Rodriguez San Miguel, D. A. Aldave, S. Diaz Tendero, M. Alcami, F. Martin, J. Gomez Herrero, and F. Zamora, Adv. Mater. **28**, 6332 (2016).
[42] F. Banhart, J. Kotakoski, and A. V. Krasheninnikov, ACS Nano **5**, 26 (2011).
[43] J. Kotakoski, A. V. Krasheninnikov, U. Kaiser, and J. C. Meyer, Phys. Rev. Lett. **106**, 105505 (2011).
[44] J. Kotakoski, A. V. Krasheninnikov, and K. Nordlund, Phys. Rev. B **74**, 245420 (2006).
[45] A. A. El-Barbary, R. H. Telling, C. P. Ewels, M. I. Heggie, and P. R. Briddon, Phys. Rev. B **68**, 144107 (2003).
[46] G.-D. Lee, C. Z. Wang, E. Yoon, N.-M. Hwang, D.-Y. Kim, and K. M. Ho, Phys. Rev. Lett. **95**, 205501 (2005).
[47] M. T. Lusk and L. D. Carr, Phys. Rev. Lett. **100**, 175503 (2008).
[48] N. Fukata, A. Kasuya, and M. Suezawa, Phys. B **308–310**, 1125 (2001).
[49] V. O. Özçelik, H. H. Gurel, and S. Ciraci, Phys. Rev. B. **88**, 045440 (2013).
[50] J. Gao, J. Zhang, H. Liu, Q. Zhang, and J. Zhao, Nanoscale **5**, 9785 (2013).
[51] G. Kresse and J. Furthmüller, Phys. Rev. B **54**, 11169 (1996).

[52] J. P. Perdew, K. Burke, and M. Ernzerhof, Phys. Rev. Lett. **77**, 3865 (1996).
[53] H. J. Monkhorst and J. D. Pack, Phys. Rev. B **13**, 5188 (1976).
[54] P. E. Blöchl, Phys. Rev. B **50**, 17953 (1994).
[55] X. L. Qi and S. C. Zhang, Rev. Mod. Phys. **83**, 1057 (2011).
[56] See Supplemental Material at http://link.aps.org/supplemental/10.1103/PhysRevMaterials.3.074005 for further details of the methods, and figures of defected two-dimensional antimonene.
[57] X. Sun, Y. Liu, Z. Song, Y. Li, W. Wang, H. Lin, L. Wang, and Y. Li, J. Mater. Chem. C **5**, 4159 (2017).
[58] C. C. Liu, W. Feng, and Y. Yao, Phys. Rev. Lett. **107**, 076802 (2011).
[59] Y. Xu, B. Yan, H. J. Zhang, J. Wang, G. Xu, P. Tang, W. H. Duan, and S. C. Cheng, Phys. Rev. Lett. **111**, 136804 (2013).
[60] T. Zhou, J. Zhang, Y. Xue, B. Zhao, H. Zhang, H. Jiang, and Z. Yang, Phys. Rev. B **94**, 235449 (2016).
[61] L. Fu, C. L. Kane, and E. J. Mele, Phys. Rev. Lett. **98**, 106803 (2007).
[62] L. Fu and C. L. Kane, Phys. Rev. B **76**, 045302 (2007).
[63] W. Liu, H. Zhang, J. Shi, Z. Wang, C. Song, X. Wang, S. Lu, X. Zhou, L. Gu, D. V. Louzguine-Luzgin, M. Chen, K. Yao, and N. Chen, Nat. Commun. **7**, 13497 (2016).